Integrated kinematic time-lapse inversion workflow leveraging full-waveform inversion and machine learning

Musa Maharramov[1], Bram Willemsen[2], Partha S. Routh[1], Emily F. Peacock[1], Mark Froneberger[2], Alana P. Robinson[2], Glenn W. Bear[3], and Spyros K. Lazaratos[2]

Abstract

We demonstrate that a workflow combining emergent time-lapse full-waveform inversion (FWI) and machine learning technologies can address the demand for faster time-lapse processing and analysis. During the first stage of our proposed workflow, we invert long-wavelength velocity changes using a tomographically enhanced version of multiparameter simultaneous reflection FWI with model-difference regularization. Short-wavelength changes are inverted during the second stage of the workflow by a specialized high-resolution image-difference tomography algorithm using a neural network. We discuss application areas for each component of the workflow and show the results of a West Africa case study.

Introduction

One challenge of conventional time-lapse processing and analysis techniques is that these methods rely on significant QA/QC efforts, survey cross-equalization, and manual parametrization. Maximizing the net present value in the current environment requires shorter 4D data turnaround times. Our objective is to fill this opportunity space with novel methodologies that can expedite and automate the delivery of interpretational 4D products without compromising their quality.

A variety of existing model- and image-space time-lapse analysis techniques lend themselves to automation but are constrained by limited resolution, repeatability requirements, and the accuracy of underlying elastodynamic modeling (Maharramov and Albertin, 2007; Chu, 2013; Shragge and Lumley, 2013; Qu and Verschuur, 2016). Model-space full-waveform inversion (FWI) methods that have no explicit requirements for data conformity across multiple acquisitions can be less sensitive to survey repeatability and can be applied in an automated inversion of time-lapse attributes requiring minimal data preprocessing (Asnaashari et al., 2012; Routh et al., 2012; Raknes et al., 2013; Willemsen and Malcolm, 2015; Alemie and Sacchi, 2016; Maharramov et al., 2016).

During the first stage of our kinematic time-lapse inversion workflow, we conduct a tomographically enhanced version of our 4D FWI method for frequencies up to 30 Hz (Maharramov et al., 2017b). This step resolves large-scale 4D velocity effects that cause time displacements in excess of the data sampling rate. During the second stage, we supply the resulting full or partial stacks to our new image-difference tomography method with a model-difference

regularization. Our approach departs from earlier image-difference tomography techniques (Maharramov and Albertin, 2007; Yang et al., 2014), since it employs a kinematic misfit functional of two images based on a neural network. The misfit functional is designed to be robust with respect to nonrepeatability and dynamic effects in the two images by training the underlying neural network on noisy synthetic data with poor repeatability. We discuss separate and joint deployment of 4D FWI and image-difference tomography in 4D projects and describe the application of our workflow to resolve gas-ex-solution (i.e., gas coming out of solution when pressure drops below the bubble point), water sweep, and pressure effects in a West Africa case study.

Theory

Kinematic FWI objective functions based on phase misfits in time and frequency domains are easily computable and yield explicit expressions for the adjoint source (Fichtner, 2011). Such phase misfits as well as the normalized L_2 objective function (Routh et al., 2011) use the phase as a proxy for traveltime information. The phase-only objective function with implicit spectral shaping (Maharramov et al., 2017a; Fu et al., 2018) fully separates kinematic and dynamic information for a single transmission or reflection event in dispersive viscoelastic media. An FWI method using a phase-misfit objective function provides true kinematic FWI when applied to refraction-only (diving-wave) data that are cleanly separated into individual events (Fichtner, 2011). While application of joint 4D FWI to diving-wave data is of potential interest for shallow anomaly identification or long-offset repeat acquisitions (Maharramov et al., 2016), our objective is 4D FWI of reflection data because of the typically limited offset range of conventional monitor acquisitions. In our approach, we use the normalized L_2 and phase-only objective functions in a tomographically enhanced reflection 4D FWI. To reduce the leakage of reflection amplitudes into the extracted phase, we use time-windowed objective functions (Maharramov et al., 2017a). The 4D FWI is preceded by the inversion of a baseline pseudodensity (with no long-wavelength density components) that populates the forward-modeled baseline data with reflections that appear at the right depth for the baseline survey. The inverted baseline pseudodensity is then supplied as a fixed parameter for baseline and monitor forward modeling and used in a joint 4D FWI with a model-difference regularization. The following sections describe this method and the subsequent step of residual image-difference tomography. This approach is similar to the one taken by

[1]ExxonMobil Upstream Research Company, Spring, Texas, USA. E-mail: musa.maharramov@exxonmobil.com; partha.routh@exxonmobil.com; emily.f.peacock@exxonmobil.com.
[2]ExxonMobil Upstream Integrated Solutions Company, Spring, Texas, USA. E-mail: bram.willemsen@exxonmobil.com; mark.froneberger@exxonmobil.com; alana.p.robinson@exxonmobil.com; spyros.lazaratos@exxonmobil.com.
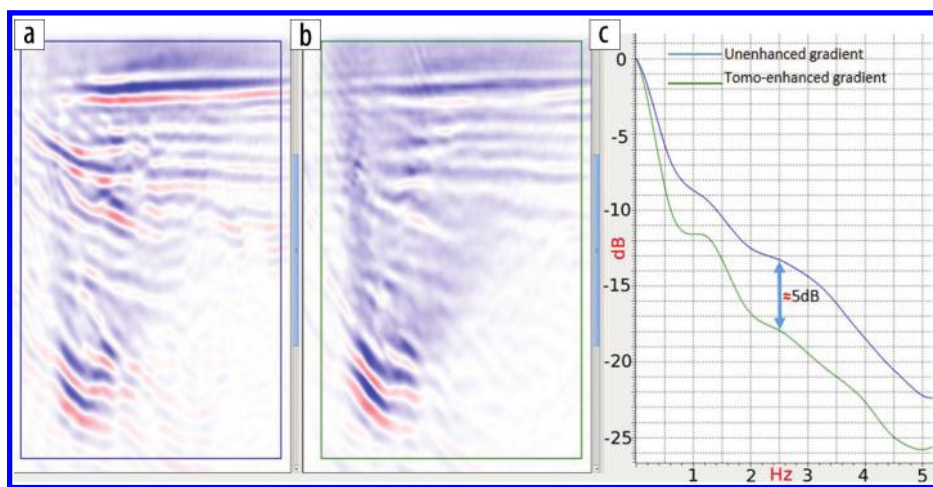[3]ExxonMobil Services and Technology, Bangalore, India. E-mail: glenn.w.bear@exxonmobil.com.

Figure 1. Monitor FWI acoustic slowness gradient of misfit equation 4 using (a) unit density and (b) a previously inverted baseline pseudodensity. (c) The log-amplitude spectrum of the gradients shows the amplitude of the tomographically enhanced gradient (green curve) decaying faster with increasing wavenumbers than that of the unenhanced gradient (blue curve). Longest-wavelength gradient components is what we need for tomography.

tomographically enhanced 3D FWI that alternately inverts short-wavelength reflectivity, or pseudodensity, and long-wavelength tomographic velocity models (Xu et al., 2012).

Tomographically enhanced joint 4D FWI

We simultaneously invert baseline and monitor models m_1 and m_2 by solving the following optimization problem (Maharramov et al., 2016):

$$(m_1, m_2) = \text{argmin } \alpha\mu[u_1, d_1] + \beta\mu[u_2, d_2] + \qquad (1)$$

$$\delta\left\|\nabla(m_2 - m_1)\right\|_1 , \qquad (2)$$

where d_1 and d_2 are the observed baseline and monitor data, u_1 and u_2 are the predicted baseline and monitor data, and α, β, and δ are the misfit and regularization weights. In an acoustic kinematic inversion, m_1 and m_2 are the baseline and monitor acoustic slownesses. The data misfit function μ in equation 1 is a measure of kinematic misfit between individual traces of the forward-modeled and observed data, summed for all source and receiver pairs. Possible choices for μ for a fixed source-receiver pair include the trace-normalized windowed L_2 misfit function (Routh et al., 2011),

$$\mu[u, d] = \int_0^T \left\|\frac{w_\tau u}{\|w_\tau u\|_2} - \frac{w_\tau d}{\|w_\tau d\|_2}\right\|_2^2 d\tau , \qquad (3)$$

computed in the time domain for each pair of forward-modeled and observed data traces $u = u(t)$ and $d = d(t)$, or the time-domain windowed phase-only objective function,

$$\mu[u, d] = \int_0^T \left\|\frac{\widetilde{w_\tau u}}{|\widetilde{w_\tau u}|} - \frac{\widetilde{w_\tau d}}{|\widetilde{w_\tau d}|}\right\|_2^2 d\tau , \qquad (4)$$

where the wide tilde represents temporal Fourier transform, and $w_\tau(t)$ is a windowing function centered at time $t = \tau$. Both objective functions can use sliding or picking windows. In nondispersive media where the background seismic Q has no significant effect on amplitudes, the objective functions of equations 3 and 4 perform similarly, while a strong uncompensated Q makes the latter a better choice. In the absence of low-frequency data and accurate dynamic modeling, reflection FWI using the objective functions of equations 3 and 4 is not true kinematic inversion unless oscillatory migration artifacts are ameliorated. However, long-wavelength time-lapse kinematic model changes can still be extracted from the inverted monitor and baseline models if the oscillatory artifacts in the two inverted models are forced to match or are penalized in their difference (Maharramov et al., 2016). This brings us to the regularization term in equation 2 of the joint 4D FWI. The anisotropic total-variation model-difference regularization in equation 2 penalizes oscillations while tolerating blocky changes with sharp boundaries. The anisotropic aspect refers to weighting blockiness differently in different directions. This reduces the leakage into the model difference of oscillatory migration artifacts, such as those in Figure 1a. The panel shows a monitor gradient computed using the objective function of equation 4 with unit background density. To reduce the sensitivity of objective functions 3 and 4 to reflectors in our tomographically enhanced 4D FWI, we conduct an FWI of baseline pseudodensity and pseudoshear velocity with one of the earlier objective functions, allowing the inverted pseudodensity to partially absorb the migration artifacts described. The resulting oscillatory model is then supplied as a common density model into the elastic modeling engine of the joint 4D FWI for baseline and monitor. This results in a stronger tomographic component in the objective function gradient, with the leakage of migration artifacts into the slowness significantly reduced — see the tomographically enhanced gradient in Figure 1b and the normalized log-amplitude spectral plots of the two gradients in Figure 1c.

Residual image-difference tomography

Total-variation regularization in the joint 4D FWI is blind to the nature of oscillations in the model difference and may penalize true fine-scale single-cycle time-lapse effects (e.g., fluid saturation changes in thin sandy intervals). Figure 2a shows a single inline cross section of the baseline migration image superimposed with the residual image-difference time shifts. The time shifts were computed between the baseline image and a monitor image. The latter was migrated using the migration velocity, which was the sum of the baseline migration velocity and the velocity difference obtained by solving the problem of equations 1 and 2. This field data application is described in the following section. The inversion was performed on a 10 m grid with frequencies up to 28 Hz. The result indicates a residual time displacement between the images

in excess of 2 ms within the reservoir (green lines). Such time shifts, while on the order of the data sampling rate for FWI, are significant in time-lapse analysis and indicate that important interpretable production effects may remain unresolved (MacBeth et al., 2019). Once the residual time shifts are reduced to a few milliseconds, we apply a regularized image-difference tomography method to further reduce the residual misalignment for interpretable results. Figure 2b shows the residual time shifts after the monitor migration velocity was updated by the output of this algorithm. The velocity was iteratively updated until the shifts within the reservoir dropped below .5 ms.

We iteratively estimate a 3D volume of time shifts $\tau = \tau\,(x,y,z)$ between the baseline and monitor images $I_1(x,y,z)$ and $I_2(x,y,z)$ migrated using the baseline and monitor imaging velocities v_1 and v_2, update the monitor imaging velocity $v_2 \leftarrow 1/(v_2^{-1} + \delta s)$ using slowness updates $\delta s(x,y,z)$ derived from the estimated time shifts, and, if necessary, remigrate the monitor with the updated velocity. The process terminates when the estimated time shifts are less than a specified value τ_{max} (e.g., .5 ms). The estimated time-shift volume $\tau(x,y,z)$ is converted to a monitor slowness update $\delta s(x,y,z)$ by solving the following optimization problem:

$$\delta s(x, y, z) = \arg\min \left\|\tau(x, y, z) - \int_\gamma \delta s\, dl\right\|_2^2 + \alpha\left\|\nabla \delta s\right\|_1, \quad (5)$$

where $\gamma = \gamma(x,y,z)$ is a line or curve segment starting at (x,y,z) and extending upward over the area of image misalignment, and dl is the element of curve length. The integration path γ points in the direction of the time-shift calculation. Note that without regularization and when γ is a vertical line segment, equation 5 reduces to the conventional process of estimating slowness updates by differentiating the time shifts (Hatchell and Bourne, 2005; MacBeth et al., 2019). The existing deterministic time-shift estimation algorithms (Rickett and Lumley, 2001; Hale, 2009, 2013) require extensive QC, conditioning, and parameter fine-tuning when used on poorly repeatable images. With cycle-time reduction as our primary objective, we sought to investigate if training an algorithm with no user-defined parameters can achieve the same or better results. First, we formulate shift estimation as a statistical classification problem (Hastie et al., 2009) by classifying pairs of N-sample random traces (or 2D/3D windowed trace gathers) shifted with respect to each other by not more than $K\Delta T$ s into $2K + 1$ classes S_i, $i = -K, ..., K$ such that the traces of each pair in the class S_i are shifted with respect to each other by
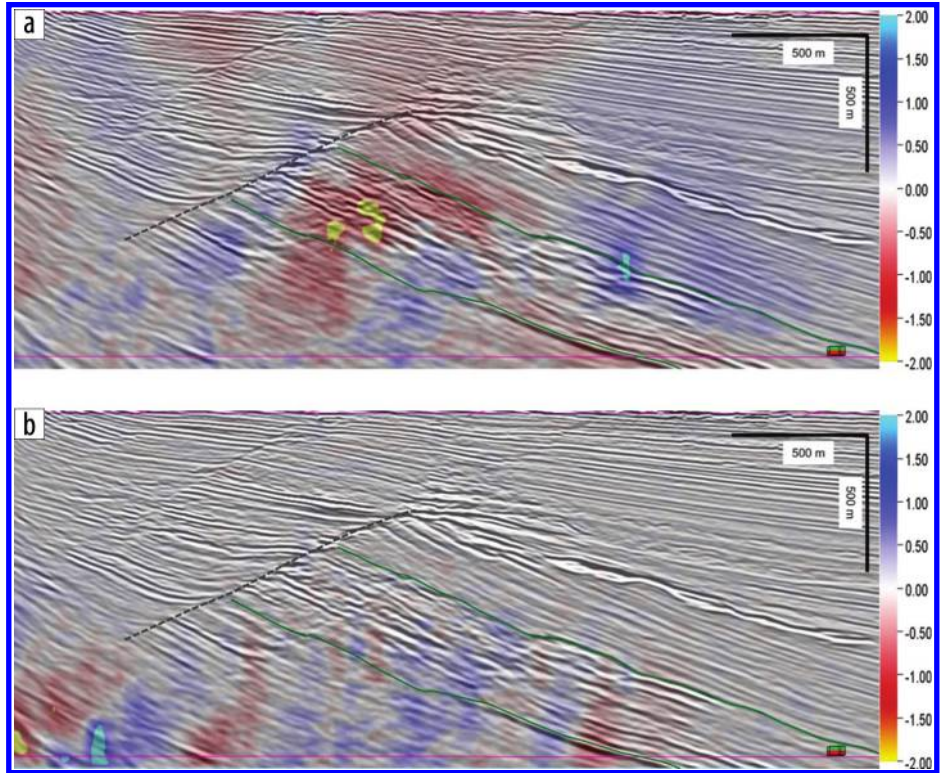

Figure 2. (a) Residual traveltime shifts (ms) after the time-lapse FWI stage of the new workflow shown in Figure 5. (b) Residual traveltime shifts (ms) after the subsequent image-difference tomography stage of the new workflow shown in Figure 5. The two green lines are the reservoir top and base.

$i\Delta T$. Classification can be done by a feed-forward neural network with a single hidden layer,

$$\mathbf{p}(\mathbf{x}) = \Sigma_2[\mathbf{z}(\mathbf{x})], \quad \mathbf{z}(\mathbf{x}) = \mathbf{w}_2 + \mathbf{W}_2\, \Sigma_1[\mathbf{w}_1 + \mathbf{W}_1\mathbf{x}], \quad (6)$$

where $\mathbf{x}$ is a column vector of $2N$ trace components from the same pair with each trace normalized by its maximum absolute value, $\mathbf{W}_1$ is an $M \times 2N$ matrix (M is the number of hidden elements $\mathbf{z}$), $\mathbf{W}_2$ is a $(2K + 1) \times M$ matrix, $\mathbf{w}_1$ is an $M \times 1$ column vector, $\mathbf{w}_2$ is a $(2K + 1) \times 1$ column vector, Σ_1 is an $M \times M$ nonlinear map consisting of element-wise application of the sigmoid activation function $1/(1+e^{-x})$ to an $M \times 1$ column vector, and Σ_2 is a $(2K + 1) \times (2K + 1)$ output map that in our case is an element-wise application of the sigmoid function. The output $(2K + 1)$ vector $\mathbf{p}$ is such that if $i^{max} = \arg\max p_i$, then the input pair of traces is shifted with respect to each other by $i^{max} \Delta T$ s. The neural network of equation 6 is trained by fitting the unknown weights $\mathbf{W}_{1,2}$ and $\mathbf{w}_{1,2}$ to a training database of trace pairs by minimizing the regularized least-squares loss function

$$\sum_{\mathbf{x} \in \text{Batch}} \left\|\mathbf{y}(\mathbf{x}) - \mathbf{p}(\mathbf{x})\right\|_2^2 + \alpha\left(\left\|\mathbf{w}_{1,2}\right\|_2^2 + \left\|\mathbf{W}_{1,2}\right\|_F^2\right), \quad (7)$$

where $\|\|_F$ is the matrix Frobenius norm, and $\mathbf{y}(\mathbf{x})$ is a $(2K + 1) \times 1$ column vector with its ith component nonzero and equal to 1 if the second trace from the pair $\mathbf{x}$ is shifted by $i\Delta T$ with respect to the first trace. To avoid parameter overfitting, training is performed on small batches of training traces that are random subsets of the training data set (Hastie et al., 2009; Keskar et al., 2016). Once the neural network has been trained and
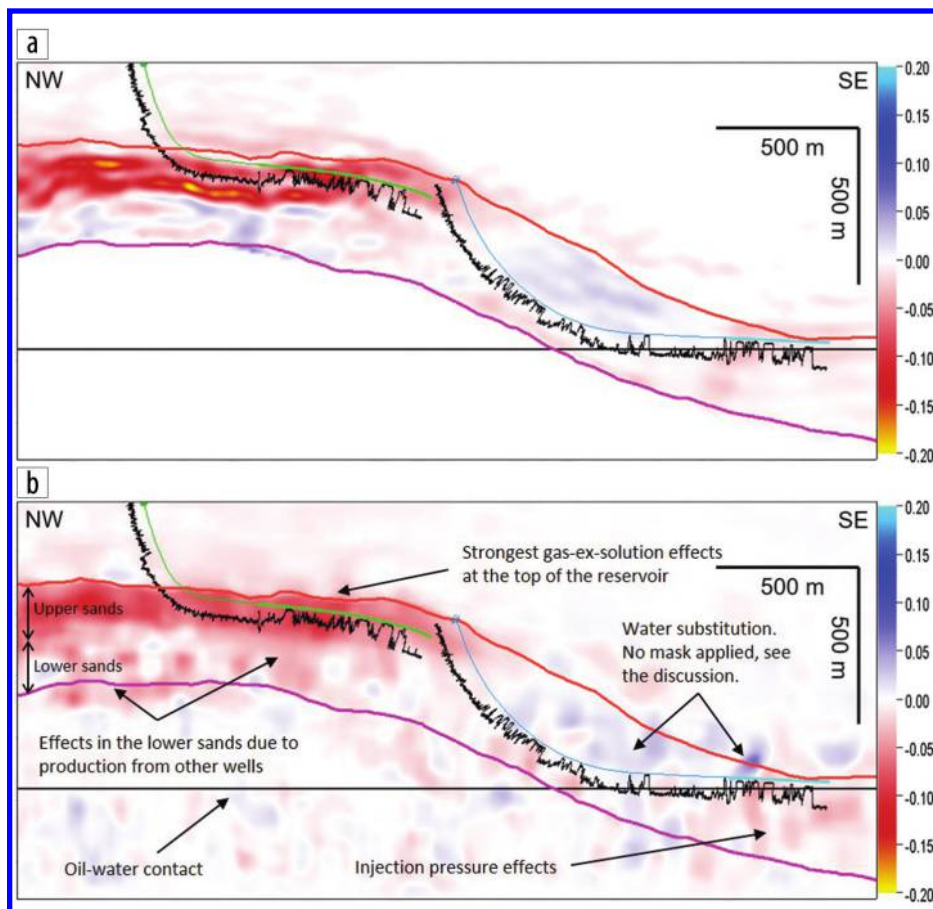
Figure 3. (a) Conventional (approximately eight-month effort) $\Delta v/v$. (b) The new workflow (approximately two-week effort) $\Delta v/v$. The green and blue segments on well trajectories mark production and injection intervals. Gas-ex-solution effects (slowdown) are present in the production well on the left. The downdip well injects water into the top sand, resulting in a water sweep (speedup) above the oil-water contact (black horizontal line) and pressure increase at the injector completion. All of the effects are well pronounced in the second panel. The producing sands are believed to be in communication, with the strongest gas effects expected near the top of the reservoir. Production and injection effects in the lower sands are caused by wells not shown here. Horizons were mapped as part of the conventional workflow. Image focusing and 1D time-shift computation impact the position of and impart noise on $\Delta v/v$. However, computing time shifts in 2D/3D windows instead of 1D as done here can ameliorate this issue.

Note that our use of neural networks is somewhat different from more common applications of machine learning in interpretation or predictive analytics (e.g., Cao and Roy, 2017). We performed a well-defined sensory task for which deterministic algorithms exist but are variously sensitive to data quality and runtime parametrization. We created a more autonomous and robust algorithm by precomputing the parameters of a general algorithmic framework that, when given suitable parameters (e.g., network weights), will perform the task. The feed-forward neural network of equation 6 provides such a framework for residual time-shift estimation.

West Africa case study

The dipping, faulted, and stacked reservoir that is the subject of our study exhibited a range of responses to production and injection between the time of the baseline survey in 2002 and the first monitor survey in 2008 (Mitchell et al., 2009). The four interconnected reservoir sand intervals are between approximately 2.0 and 2.5 km deep (delineated by the top and bottom horizons in Figures 3a and 3b). Pressure drawdown below the bubble point led to the gas coming out of solution, causing large acoustic velocity decreases near the reservoir top (marked by the top horizon). Water injection into the reservoir sands and aquifer movement led to velocity increases due to a larger water saturation above the oil-water contact and velocity decreases due to effective stress drop (pore pressure increase) below injector completions.

As the first step of our workflow, we applied the tomographically enhanced reflection 4D FWI method described earlier. The inversion started from a smooth baseline imaging velocity model produced using conventional tomography, with the anisotropy parameters fine-tuned to achieve improved well ties. FWI was conducted using approximately 1500 baseline and monitor shot gathers, supplied separately into the two FWI misfit functions of equation 1. The shots were picked randomly from the two surveys after surface-related multiple elimination and debubble processing with no repeatability constraints on their geometry. A time-domain FWI was conducted on 28 Hz data that was spectrally shaped to speed up the convergence (Lazaratos et al., 2011). The 4D FWI resolved the long-wavelength velocity changes associated with gas-ex-solution effects, bringing the residual time shifts between migrated baseline and monitor images from over 30 ms to 2–4 ms, as shown in Figure 2a. To resolve more subtle effects, we conducted the image-difference tomography of nonequalized raw images on a 3 m grid until the time shifts dropped below .5 ms in the reservoir and overburden (Figure 2b). No QC of

adequate testing accuracy has been achieved, it can be used to produce the mathematical expectation of a shift (i.e., predict a continuous attribute):

$$\tau = \sum_{i=-K}^{K} \frac{z_i - z_{\min}}{\sum_{j=-K}^{K} z_j - z_{\min}} i\Delta T, \qquad (8)$$

where the $(2K + 1) \times 1$ vector $\mathbf{z}$ is the output of the second network layer before the final activation functions are applied in equation 6.

The neural network of this example was trained on a database of 90,000 pairs of 61-sample random traces ($N = 61$ in equation 6). The traces were generated using a convolutional model of band-limited reflectivity, with 10% random amplitude errors and 10% random Gaussian noise added to imitate nonrepeatability. The hyperparameters (the number of hidden elements $M = 150$ in equation 6 and the regularization weight $\alpha = .1$ in equation 7) were identified experimentally to achieve acceptable trade-off between the model bias and training error. The dominant frequency of the synthetic traces was a quarter of the Nyquist frequency. The training traces had relative shifts ranging from −3 to +3 samples with the granularity of half a sample.

migrated images or estimated time shifts was performed at any stage of the image-difference tomography, thus speeding up the process and reducing costs when compared with conventional workflows. The resulting difference of monitor and baseline acoustic velocities, shown in Figure 3b, is in good agreement with the well information (see the producer on the left and injector on the right). The result is also in agreement with the conventional $\Delta v/v$ product shown in Figure 3a. The maximum absolute-value attribute maps for the top reservoir sand are shown in Figure 4 for a conventional 4D image difference, conventional $\Delta v/v$, and the $\Delta v/v$ produced using the new automated workflow. The conventional image difference, as an amplitude-based method, has greater theoretical sensitivity to 4D effects than that of purely kinematic methods. However, note its conformance with our kinematic product near the oil-water contact. Our research is continuing with the objective of extending the workflow to deliver time-lapse amplitude products.

Discussion

We developed a workflow that significantly reduces 4D processing times and costs, leading to increased value of time-lapse data. Figure 5 contrasts the proposed 4D FWI and machine learning workflow with a typical conventional counterpart. We reduce processing times and costs by eliminating conventional

premigration processing, image cross-equalization, and time-shift conditioning, which are among the most time-consuming stages of conventional workflows. Products delivered by the new workflow are ready within weeks of demultiple processing, significantly shortening 4D cycle times. Limiting FWI to coarse grids keeps it within the contemporary range of easy computability. Specializing the tomographic step in resolving subtle effects keeps down the costs of training robust neural networks. Both methods can be applied
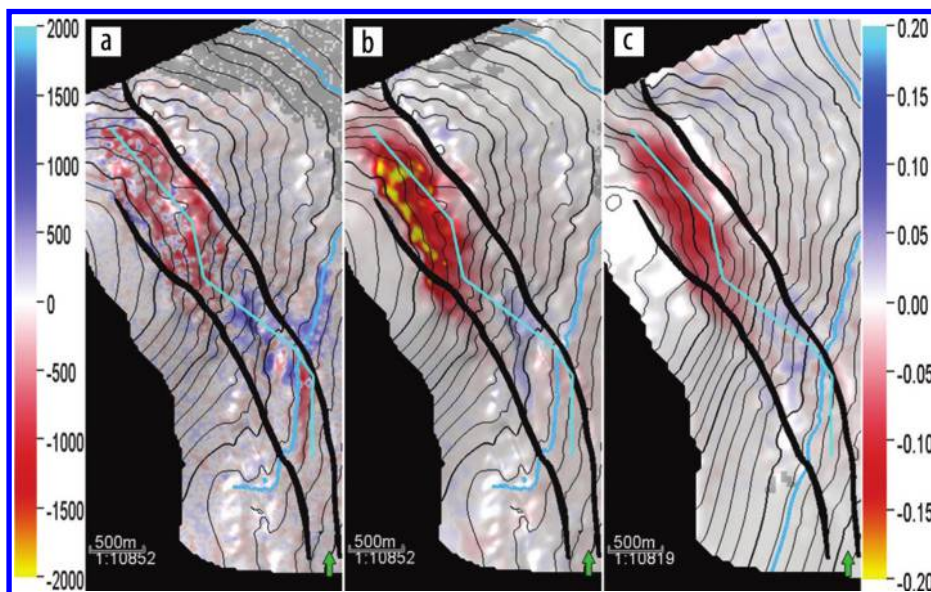

Figure 4. Top sand maximum absolute-value attribute extractions from (a) the conventional image difference, (b) conventional $\Delta v/v$, and (c) the new workflow $\Delta v/v$ (displayed at the same scale as the conventional $\Delta v/v$). Note the production-related slowdown effect near the crest of the structure, downdip speedup above the oil-water contact (blue line), and the slowdown below the oil-water contact. All three effects are evident in the image difference and new $\Delta v/v$ products. The light-blue line shows the cross section of Figures 3a and 3b.
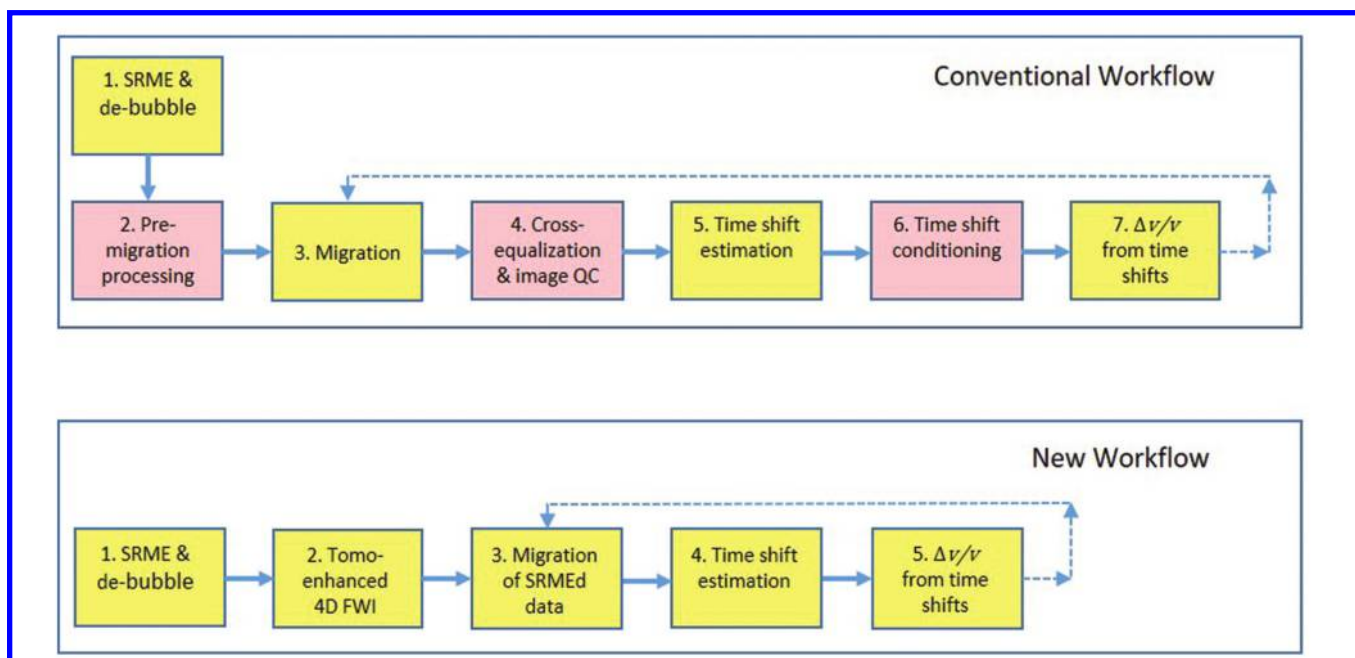

Figure 5. A typical conventional workflow versus the proposed integrated 4D FWI and machine learning workflow. Our workflow reduces processing time by eliminating conventional premigration processing, image (stack) cross-equalization, conditioning of time shifts, and associated QC (steps 2, 4, and 6 in the first workflow). This is achieved through the application of 4D FWI to resolve large time shifts directly from minimally processed data and the application of machine learning to extract small residual time shifts from nonequalized raw images. Both workflows can feature multiple passes of time-shift extraction and $\Delta v/v$ estimation until the residual time shifts are below a certain threshold, with the new workflow performing all steps in an automated loop.

standalone or jointly, without any cross-equalization or processing beyond the needs of basic imaging. The combined workflow can match or exceed the value of conventional $\Delta v/v$ using only minimally processed data and raw images. **TLE**

Acknowledgments

Data and materials availability

Data associated with this research are confidential and cannot be released.

Corresponding author: musa.maharramov@exxonmobil.com

References

Alemie, W., and M. Sacchi, 2016, Joint reparametrized time-lapse full-waveform inversion: 86th Annual International Meeting, SEG, Expanded Abstracts, 1309–1314, https://doi.org/10.1190/segam2016-13879371.1.

Asnaashari, A., R. Brossier, S. Garambois, F. Audebert, P. Thore, and J. Virieux, 2012, Time-lapse imaging using regularized FWI: A robustness study: 82nd Annual International Meeting, SEG, Expanded Abstracts, https://doi.org/10.1190/segam2012-0699.1.

Cao, J., and B. Roy, 2017, Time-lapse reservoir property change estimation from seismic using machine learning: The Leading Edge, **36**, no. 3, 234–238, https://doi.org/10.1190/tle36030234.1.

Chu, D., 2013, Estimating reservoir properties from 4D seismic data: U.S. Patent 2013/0060475 A1.

Fichtner, A., 2011, Full seismic waveform modelling and inversion: Springer.

Fu, L., B. Guo, and G. T. Schuster, 2018, Multiscale phase inversion of seismic data: Geophysics, **83**, no. 2, R159–R171, https://doi.org/10.1190/geo2017-0353.1.

Hale, D., 2009, A method for estimating apparent displacement vectors from time-lapse seismic images: Geophysics, **74**, no. 5, V99–V107, https://doi.org/10.1190/1.3184015.

Hale, D., 2013, Dynamic warping of seismic images: Geophysics, **78**, no. 2, S105–S115, https://doi.org/10.1190/geo2012-0327.1.

Hastie, T., R. Tibshirani, and J. Friedman, 2009, The elements of statistical learning: Data mining, inference, and prediction, second edition: Springer.

Hatchell, P., and S. Bourne, 2005, Measuring reservoir compaction using time-lapse timeshifts: 75th Annual International Meeting, SEG, Expanded Abstracts, 2500–2503, https://doi.org/10.1190/1.2148230.

Keskar, N. S., D. Mudigere, J. Nocedal, M. Smelyanskiy, and P. T. P. Tang, 2016, On large-batch training for deep learning: Generalization gap and sharp minima: arXiv:1609.04836.

Lazaratos, S., I. Chikichev, and K. Wang, 2011, Improving the convergence rate of full wavefield inversion using spectral shaping: 81st Annual International Meeting, SEG, Expanded Abstracts, 2428–2432, https://doi.org/10.1190/1.3627696.

MacBeth, C., M.-D. Mangriotis, and H. Amini, 2019, Review paper: Post-stack 4D seismic time-shifts: Interpretation and evaluation: Geophysical Prospecting, **67**, no. 1, 3–31, https://doi.org/10.1111/1365-2478.12688.

Maharramov, M., and U. Albertin, 2007, Localized image-difference wave-equation tomography: 77th Annual International Meeting, SEG, Expanded Abstracts, 3009–3013, https://doi.org/10.1190/1.2793096.

Maharramov, M., A. I. Baumstein, Y. Tang, P. S. Routh, S. Lee, and S. K. Lazaratos, 2017a, Time-domain broadband phase-only full-waveform inversion with implicit shaping: 87th Annual International Meeting, SEG, Expanded Abstracts, 1297–1301, https://doi.org/10.1190/segam2017-17744416.1.

Maharramov, M., B. L. Biondi, and M. A. Meadows, 2016, Time-lapse inverse theory with applications: Geophysics, **81**, no. 6, R485–R501, https://doi.org/10.1190/geo2016-0131.1.

Maharramov, M., G. Chen, P. S. Routh, A. I. Baumstein, S. Lee, and S. K. Lazaratos, 2017b, Multiscale time-domain time-lapse full-waveform inversion with a model-difference regularization: 87th Annual International Meeting, SEG, Expanded Abstracts, 1428–1433, https://doi.org/10.1190/segam2017-17743726.1.

Mitchell, P., R. Paez, D. Johnston, G. Mohler, and C. da Cunha Neto, 2009, 4D seismic in deep water at the Dikanza field, offshore Angola, West Africa: 79th Annual International Meeting, SEG, Expanded Abstracts, 3924–3928, https://doi.org/10.1190/1.3255688.

Qu, S., and D. Verschuur, 2016, Getting accurate time-lapse information using geology-constrained simultaneous joint migration-inversion: 86th Annual International Meeting, SEG, Expanded Abstracts, 5451–5456, https://doi.org/10.1190/segam2016-13964374.1.

Raknes, E., W. Weibull, and B. Arntsen, 2013, Time-lapse full waveform inversion: Synthetic and real data examples: 83rd Annual International Meeting, SEG, Expanded Abstracts, 944–948, https://doi.org/10.1190/segam2013-0540.1.

Rickett, J. E., and D. E. Lumley, 2001, Cross-equalization data processing for time-lapse seismic reservoir monitoring: A case study from the Gulf of Mexico: Geophysics, **66**, no. 4, 1015–1025, https://doi.org/10.1190/1.1487049.

Routh, P., G. Palacharla, I. Chikichev, and S. Lazaratos, 2012, Full wavefield inversion of time-lapse data for improved imaging and reservoir characterization: 82nd Annual International Meeting, SEG, Expanded Abstracts, 1–6, https://doi.org/10.1190/segam2012-1043.1.

Routh, P. S., J. R. Krebs, S. Lazaratos, A. I. Baumstein, I. Chikichev, N. Downey, D. Hinkley, and J. E. Anderson, 2011, Full-wavefield inversion of marine streamer data with the encoded simultaneous source method: Presented at the 73rd Conference and Exhibition, EAGE.

Shragge, J., and D. Lumley, 2013, Time-lapse wave-equation migration velocity analysis: 22nd Geophysical Conference, ASEG, 1–5, https://doi.org/10.1071/ASEG2012ab197.

Willemsen, B., and A. Malcolm, 2015, Regularizing velocity differences in time-lapse FWI using gradient mismatch information: 85th Annual International Meeting, SEG, Expanded Abstracts, 5384–5388, https://doi.org/10.1190/segam2015-5908610.1.

Xu, S., D. Wang, F. Chen, G. Lambaré, and Y. Zhang, 2012, Inversion on reflected seismic wave: 82nd Annual International Meeting, SEG, Expanded Abstracts, 1–7, https://doi.org/10.1190/segam2012-1473.1.

Yang, D., A. Malcolm, and M. Fehler, 2014, Using image warping for time-lapse image domain wavefield tomography: Geophysics, **79**, no. 3, WA141–WA151, https://doi.org/10.1190/geo2013-0424.1.